Optics EXPRESS

Revealing a one-dimensional optically cloaked surface using the spin Hall effect of light

MINKYUNG KIM[1,*] AND DASOL LEE[2]

[1] *School of Mechanical Engineering, Gwangju Institute of Science and Technology (GIST), Gwangju 61005, Republic of Korea*
[2] *Department of Biomedical Engineering, Yonsei University, Wonju 26493, Republic of Korea*
[*] *m.kim@gist.ac.kr*

Abstract: The realization of an optical cloak that can hide a target object is no longer fiction, yet distinguishing the optically cloaked surface from our illusion remains an open problem. Here, the detection of a one-dimensional optically cloaked surface is presented by leveraging the spin Hall effect of light, the microscopic and transverse splitting of linearly polarized light at an optical interface into two circular polarizations. We first derive an analytical formula for the spin Hall shift at a planar surface with a linear phase gradient and demonstrate that the spin Hall effect of light at the cloaked surface differs from that at its perceived image. The theoretical description and numerical computation are generalized for a curved surface with a nonlinear phase gradient. Two approaches for examining optically cloaked surfaces are presented, in which the unknown incident angle and phase gradient are successfully reproduced. This work suggests the potential of the spin Hall effect of light in various applications, including anti-counterfeiting and security.

1. Introduction

Recent advances in optics and nanofabrication have brought the concept of invisibility cloaks into reality by manipulating the amplitude and phase of electromagnetic waves using artificially designed structures [1–7]. Among the various methods, the most efficient is the skin cloak [8], which renders an object with an arbitrary geometrical shape invisible by compensating the phase using subwavelength-thick metasurfaces. Patterned on the surface of an arbitrarily shaped three-dimensional object, the metasurface introduces an additional height-dependent phase so that the observer perceives the object as flat [9]. Early cloaking devices operated under limited conditions, that is, under a specific azimuth angle, polarization, and limited wavelength regime. However, considerable efforts to alleviate the operation conditions have enabled optical cloaks that can hide objects under polarization insensitivity [10,11] or broadband light [12–14] and dynamic tunability [15,16], self-adaptivity [17], etc.

As optical cloaking evolves, the importance of developing a technique to reveal cloaked objects has grown. This study begins with the question: If an ideal skin cloak that perfectly conceals an object underneath it exists, how can one distinguish the cloaked surface from its uncloaked counterpart? Here, we demonstrate that an ideal skin-cloaked surface with a one-dimensional (1D) phase gradient can be revealed by exploiting the spin Hall effect of light (SHEL) [18–23]. Because the amount of splitting or so-called spin Hall shift is closely linked to the Fresnel coefficients and incident angle [24–36] and can be measured precisely via weak measurement [19,37], the SHEL has been used as a measurement pointer to identify unknown parameters at an interface, such as the refractive index and number of layers [37–42] and has proven its potential in detecting geometrical [43], chemical [44], and biological [45,46] features. However, despite its versatility in detecting and sensing applications, SHEL has not yet been used to detect optically cloaked regions.

While the detection using the SHEL in previous studies has thus far relied on the changes in the Fresnel coefficients, the identification of the cloaked surface introduced here is underpinned

#477099 https://doi.org/10.1364/OE.477099
Journal © 2022 Received 2 Oct 2022; revised 8 Nov 2022; accepted 9 Nov 2022; published 28 Nov 2022

by the inequality of the incident and reflected angles and its relation to the spin Hall shift. We first derive the analytic formula for the spin Hall shift at a planar surface with a linear phase gradient and confirm its validity using numerical simulations. Subsequently, its generalization to detect a curved surface with a nonlinear phase gradient is introduced. The spatially nonuniform 1D height profile is fully restored by examining the transverse displacement along the reflected beam line segment. Moreover, two methods to reproduce the unknown incident angle and phase gradient are introduced, one by comparing the SHEL at the cloaked surface and that at its uncloaked counterpart and the other by measuring the SHEL at the cloaked surface under two linear polarizations. The incident angle and phase gradient are successfully estimated from the SHEL at the planar and curved cloaked surfaces, demonstrating that the SHEL can reveal the 1D ideal skin cloak. We believe that this work expands the practicality and potential of SHEL in diverse areas, such as anti-counterfeiting and security applications.

2. Results and discussion

2.1. Spin Hall effect of light at a spatially uniform planar interface

SHEL refers to the microscopic and transverse spin-dependent splitting of light at an optical interface [18–20] (Fig. 1(a)). A linearly polarized incidence is split into two circularly polarized components, left circularly polarized (LCP) and right circularly polarized (RCP), in half, along the direction perpendicular to the incident plane (Fig. 1(b)) through the refraction/reflection as a result of the vectorial and transverse nature of light. Before deriving the analytic formula for the spin Hall shift at the cloaked surface, we first revisit the reflection of a Gaussian beam at a planar interface characterized by spatially uniform Fresnel reflection coefficients (r_p and r_s for p and s polarizations, respectively). A Gaussian beam propagating along the z_I-axis in the z_I-x_I plane is considered (see Fig. 1(c) for coordinate definitions). The spatial profile of the reflected beam can be obtained using the Fourier transform:

$$\tilde{\boldsymbol{\psi}}_{R,c}(\vec{r}) = \iint \boldsymbol{\psi}_{R,c}(\vec{k}_R)\exp(i\vec{k}_R\cdot\vec{r})dk_{Rx}dk_{Ry}, \tag{1}$$

of the reflected beam in the momentum space,

$$\boldsymbol{\psi}_{R,c}(\vec{k}_R) = M_{\boldsymbol{\psi}_R\rightarrow\boldsymbol{\psi}_{R,c}}\mathcal{J}(\vec{k}_I)M_{\boldsymbol{\psi}_{I,c}\rightarrow\boldsymbol{\psi}_I}\boldsymbol{\psi}_{I,c}(\vec{k}_I), \tag{2}$$

where the subscripts I and R denote the incident and reflected beams, respectively, and the second subscript c indicates that the quantity is expressed in the central frame.

$$\mathcal{J}(\vec{k}_I) = \begin{pmatrix} r_p(\vec{k}_I) & 0 \\ 0 & r_s(\vec{k}_I) \end{pmatrix} \tag{3}$$

is the Jones matrix that transforms the incidence to the reflected beam in the local frame ($\boldsymbol{\psi}_I \rightarrow \boldsymbol{\psi}_R$),

$$M_{\boldsymbol{\psi}_R\rightarrow\boldsymbol{\psi}_{R,c}} = \begin{pmatrix} 1 & \frac{k_y}{k_0}\frac{\cos\theta_R}{\sin\theta_I} \\ -\frac{k_y}{k_0}\frac{\cos\theta_R}{\sin\theta_I} & 1 \end{pmatrix} \tag{4}$$

is a coordinate transformation matrix of the reflected beam from the local frame to the central frame ($(\tilde{x}_R,\ \tilde{y}_R,\ \tilde{z}_R) \rightarrow (x_R,\ y_R,\ z_R)$, $\boldsymbol{\psi}_R(\vec{k}_R) \rightarrow \boldsymbol{\psi}_{R,c}(\vec{k}_R)$), where θ_I and θ_R are the incident and reflected angles, respectively. Note that $k_{Iy} = k_{Ry} \equiv k_y$ and k_0 is the wave number.

$$M_{\boldsymbol{\psi}_{I,c} \to \boldsymbol{\psi}_I} = \begin{pmatrix} 1 & \frac{k_y}{k_0} \cot \theta_I \\ -\frac{k_y}{k_0} \cot \theta_I & 1 \end{pmatrix} \tag{5}$$

is a coordinate transformation matrix of the incident beam from the central to the local frame [47] ($(x_I,\ y_I,\ z_I) \longrightarrow (\tilde{x}_I,\ \tilde{y}_I,\ \tilde{z}_I)$, $\boldsymbol{\psi}_{I,c}(\vec{k}_I) \longrightarrow \boldsymbol{\psi}_I(\vec{k}_I)$), and

$$\boldsymbol{\psi}_{I,c}(\vec{k}_I) = \frac{w_0}{\sqrt{2\pi}} \begin{pmatrix} \psi_I^H \\ \psi_I^V \end{pmatrix} \exp \left[-\frac{w_0^2}{4} (k_{Ix}^2 + k_{Iy}^2) \right] \tag{6}$$

is the incident Gaussian beam, where the superscripts H and V represent the horizontal and vertical components, respectively, and w_0 is the beam waist. At this spatially uniform interface, $\theta_I = \theta_R$ according to Snell's law, and thus, Eqs. (4) and (5) become the same. By incorporating the wave vector deflection parallel to the incident plane using a first-order Taylor expansion,

$$r_{p,s}(k_{Ix}) = r_{p,s}(k_{Ix} = 0) + k_{Ix} \frac{\partial r_{p,s}(k_{Ix})}{\partial k_{Ix}} \Big|_{k_{Ix}=0}. \tag{7}$$

The spatial profile of the reflected Gaussian beam (Eq. (1)) can be fully expressed, from which the spin Hall shift can be obtained as

$$\delta_H^{\pm} / \lambda = \mp \frac{\cot \theta_I}{2\pi} \mathrm{Re} \Big(1 + \frac{r_s^0}{r_p^0} \Big), \tag{8a}$$

$$\delta_V^{\pm} / \lambda = \mp \frac{\cot \theta_I}{2\pi} \mathrm{Re} \Big(1 + \frac{r_p^0}{r_s^0} \Big), \tag{8b}$$

by taking a y position average of the intensity in the x_R–y_R plane [33,47,48]. The superscripts + and − correspond to the LCP and RCP components, respectively. Note that Eq. (8) assumes that the beam waist is sufficiently larger than the wavelength, i.e., $k_0^2 w_0^2 \gg \cot^2 \theta_I$. This assumption is satisfied in most instances except for a tightly confined beam under near-normal incidence. In this large beam waist regime, the in-plane wave vector deflection does not affect the SHEL, as manifested by the absence of the derivatives of $r_{p,s}$ in Eq. (8). Indeed, the coupling of x and y coordinate components vanishes in this regime [37]. This implies that the SHEL, which is the splitting along the y-axis, is attributed only to its canonical conjugate k_y and the two beams reflected at different x positions reach different x_R values at a given z_R.

The origin of the SHEL can be understood as a combination of three contributions: (i) local rotation of the polarization basis at the interface, (ii) polarization-dependent transmission/reflection under oblique incidence, and (iii) reorientation of the central wave vector. The first originates from the finite beam waist of the incident Gaussian beam, which enforces the existence of deflected wave vector components that are not parallel to the incident plane. The local transformation between the deflected wave vector and the central wave vector results in a local polarization difference; that is, a purely p-polarized incidence may have s-polarized components locally (Fig. 1(f), (i) and (iii)). This contribution is described solely by the incidence itself, such as θ_I (Eq. (5)), and is irrelevant to the interface properties.

The second rescales the two polarization components (manifested in Eq. (3)) and consequently largely affects the spin Hall shift. More specifically, p- and s-polarized components of the incident beam at the optical interface are rescaled by r_p and r_s, respectively (Fig. 1(f), (ii) and (iv)). For example, suppose a p-polarized incidence is injected into an interface with r_s dominant

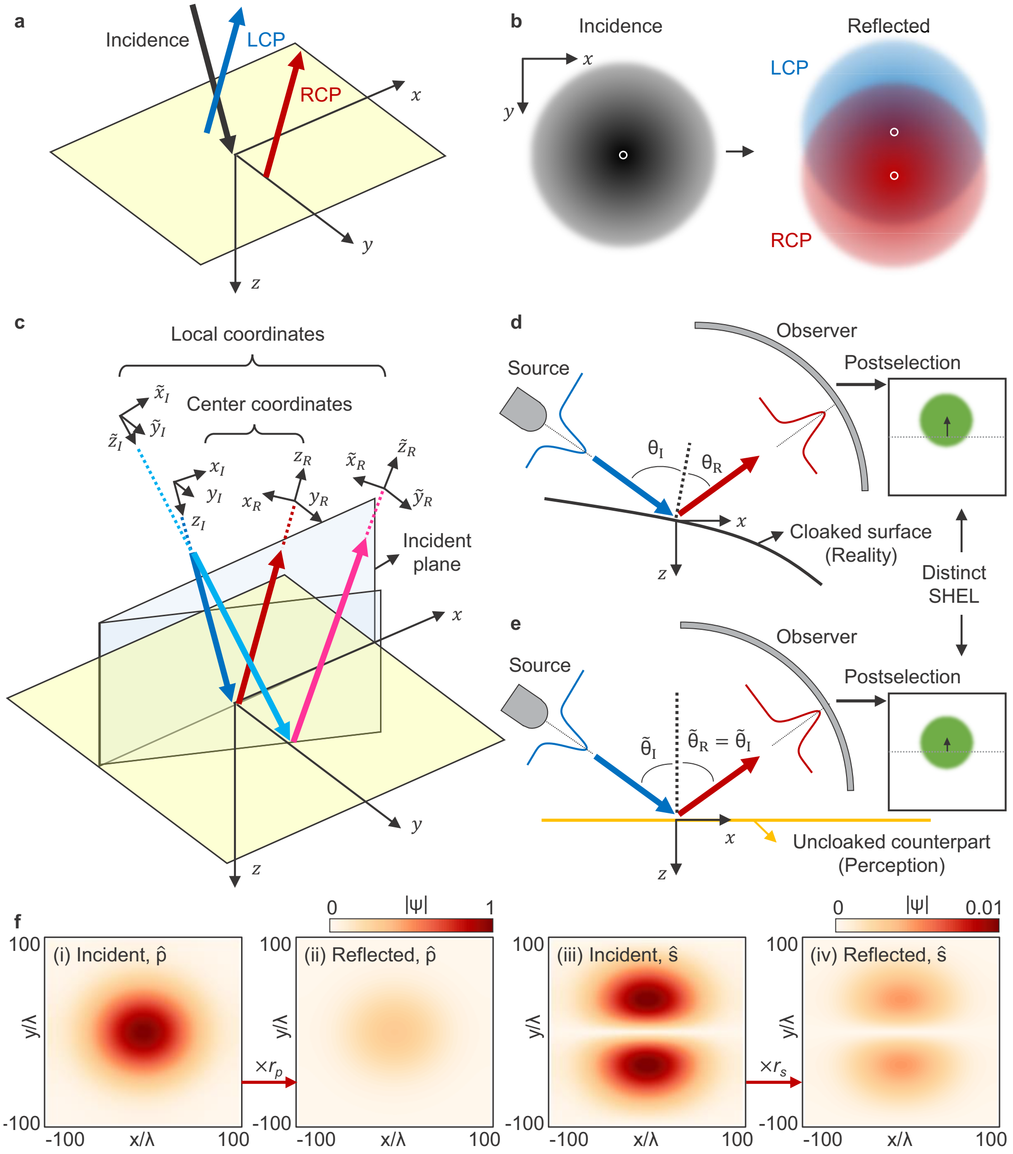

Fig. 1. SHEL-based detection of a cloaked surface. (a) Schematic of the SHEL and (b) beam profile of incident and reflected beams. (c) Microscopic illustration of Gaussian beam reflection with central (blue for incident and red for reflected beam, respectively) and noncentral (light blue for incident and magenta for reflected beam, respectively) wave vector components. The center and local coordinates follow the directions of the central and noncentral wave vectors, respectively. (d, e) Illustration of reflection at (d) a cloaked surface and (e) its uncloaked counterpart. Only the central wave vectors are plotted. (f) Spatial field profiles of the *p*- and *s*-polarized components of the incident and reflected beams at the optical interface.

over r_p. The relative strength of the s-polarized components to the p-polarized components will be significantly enhanced, leading to a large SHEL. Naturally, the overall field strength can be treated as a constant term and does not affect the SHEL; therefore, only the relative ratio between the Fresnel coefficients is important. This implies that if the Fresnel coefficients of p and s polarizations have the same additional phase gradient for polarization-independent skin cloaking, the two contributions are canceled out and have zero net effect in this rescaling process.

The last contribution usually appears only in transmission, particularly when the input and output media are different, as are the incident and transmitted angles ($\theta_I \neq \theta_T$). If the angles are different, the local rotation in the transmitted/reflected beam is different from that in the incidence. This can be understood as the inequality of Eqs. (4) and (5). However, as $\theta_I \neq \theta_R$ on the cloaked surface, this contribution survives and affects the spin Hall shift of the reflected beam. Considering that the polarization-insensitive phase terms are canceled out in the second contribution, the third one, that is, the inequality of θ_I and θ_R, is the only factor that differentiates the SHEL at the cloaked surface from that at the uncloaked counterpart.

2.2. Spin Hall effect of light at a planar surface with a linear phase gradient

During the derivation of Eq. (8), $\theta_I = \theta_R$ is used. Therefore, whereas a cloaked surface with an additional phase term and $\theta_I \neq \theta_R$ (Fig. 1(d)) cannot be visually distinguished from its perception (Fig. 1(e)) via a simple observation, the SHEL of the cloaked surface appears different from that of the uncloaked counterpart. In this and the following sections, the SHEL at a planar surface with a linear phase gradient (Figs. 2(a) and (b)) and that at a curved surface with a nonlinear phase gradient (Figs. 2(c) and (d)) are explored, respectively.

Now, we imagine a cloaked surface with a 1D linear phase gradient along the x-axis, i.e., $r_{p,s}(\vec{k}_I, \vec{r}) = r^0_{p,s}(\vec{k}_I)e^{i\phi x}$ where ϕ is a constant. Note that the direction along which the phase gradient is defined is parallel to the incident plane in our study. The additional phase term $e^{i\phi x}$ introduces the translation along the k_{Rx}-axis by ϕ as $\boldsymbol{\psi}_R(\vec{k}_R) = \boldsymbol{\psi}^0_R(\vec{k}_R - \phi\hat{k}_x)$, where $\boldsymbol{\psi}_R(\vec{k}_R)$ is the reflected beam in the local momentum space and $\boldsymbol{\psi}^0_R(\vec{k}_R)$ is the same without the phase gradient. This can be understood as the anomalous reflection induced by the phase gradient, also known as generalized Snell's law [9], $k_{Rx} - k_{Ix} = \phi$ (Fig. 2(a)). This phase continuity equation results in inequality between the incident and reflected angles.

$$\theta_R = \sin^{-1}\left(\sin\theta_I + \frac{\phi}{k_0}\right), \tag{9}$$

where θ_I and θ_R are defined with respect to the normal vector of the interface and are constants throughout the interface (Fig. 2(a)). Note that θ_I and θ_R are determined by the local slope angle of the cloaked surface and the incidence's propagation direction. The inequality of the incident angle reflected angles originating from the phase gradient should be distinguished from the angular Goos-Hänchen and Imbert-Fedorov shifts [49]. This polarization-independent phase gradient only alters the propagation direction of the reflected beam but preserves the remaining characteristics of the local reflected beam, such as the two-dimensional field profile in the x_R–y_R plane. Therefore, without further information, the observer perceives the cloaked surface (Fig. 1(d)) as its uncloaked counterpart and the incident angle as $\tilde{\theta}_I = (\theta_I + \theta_R)/2$ (Fig. 1(e)).

However, the spin Hall shift at the cloaked surface is distinct from that at the uncloaked counterpart. Similar to the derivation of Eq. (8), taking the y position average of the reflected beam in the x_R-y_R plane in the circular polarization basis gives an analytic formula for the spin Hall shift as

$$\delta^{\pm}_H/\lambda = \mp\frac{\cot\theta_I}{2\pi}\mathrm{Re}\left(\frac{\cos\theta_R}{\cos\theta_I} + \frac{r^0_s}{r^0_p}\right), \tag{10a}$$

$$\delta^{\pm}_V/\lambda = \mp\frac{\cot\theta_I}{2\pi}\mathrm{Re}\left(\frac{\cos\theta_R}{\cos\theta_I} + \frac{r^0_p}{r^0_s}\right), \tag{10b}$$

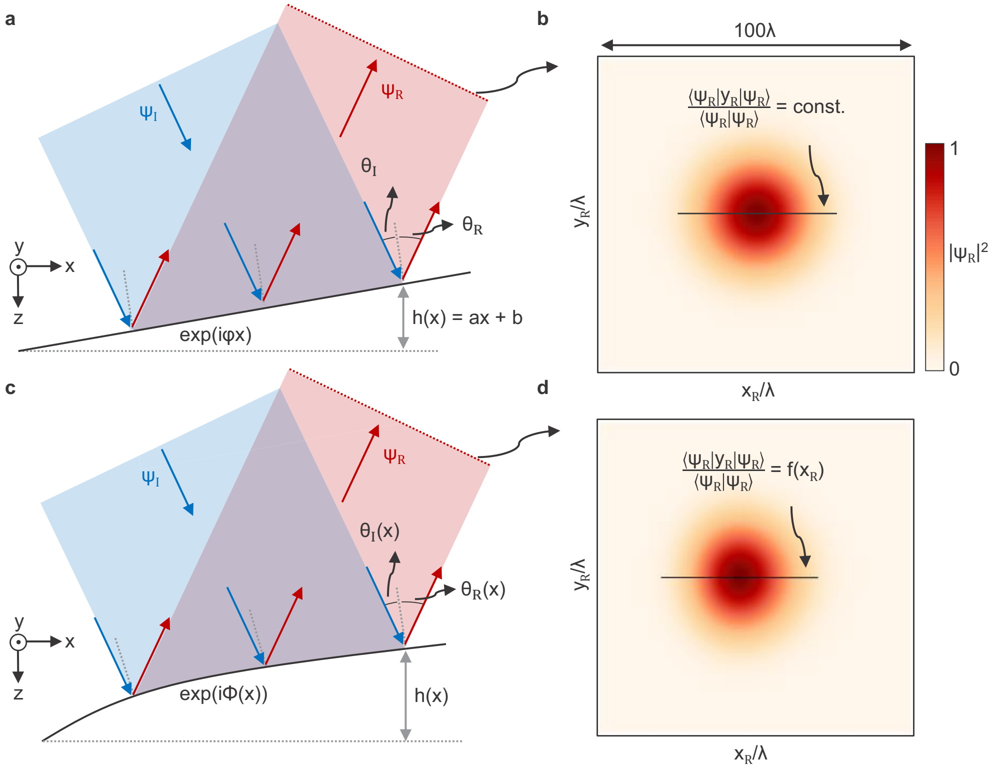

Fig. 2. SHEL at planar and curved cloaked surfaces. (a) Illustration of reflection at a planar surface with linear phase gradient and (b) the reflected beam profile. (c) Illustration of reflection at a curved surface with nonlinear phase gradient and (d) the reflected beam profile. y position average of the 1D intensity profile at each x_R is a constant for (b) and is a function of x_R for (d).

when $k_0^2 w_0^2 \gg \cot^2\theta_I$ is satisfied. The only difference between the derivation of Eq. (10) and that of Eq. (8) is that $\theta_I = \theta_R$ is used in the latter case, but not in the former. A typical profile of the reflected beam is shown in Fig. 2(b). In the absence of a phase gradient ($\phi = 0$ and thus $\theta_I = \theta_R$), Eq. (10) reduces to the well-known formula of the spin Hall shift (Eq. (8)).

2.3. Generalization to a curved surface with a nonlinear phase gradient

Equation (10) can be generalized to a curved surface with a nonlinear phase gradient, $r_{p,s}(\vec{k}_I, \vec{r}) = r^0_{p,s}(\vec{k}_I)e^{i\Phi(x)}$ (Fig. 2(c)). In such a case, the normal vector of the curved surface is defined locally and varies along the x-axis. Then, θ_I and θ_R, which are defined in terms of local normals, are not constant but are functions of x. This causes the transformation between the local and central frames (Eqs. (4) and (5)) to be defined in both $\vec{k}$- and $\vec{r}$-spaces, whereas they are defined purely in $\vec{k}$-space for the linear phase gradient case. Because the operations in $\vec{k}$- and $\vec{r}$-spaces are in terms of k_y and x, respectively, which are not a canonically conjugated pair, two operations can be performed separately. Furthermore, considering that the deviation of the incident and reflected angles of the deflected beams affects only the in-plane displacement but not the transverse displacement and that the x_R position of the reflected beam has a one-to-one correspondence to the x position at the interface, the SHEL can be obtained following a similar procedure but x-dependently (Fig. 2(d)). More specifically, y position average of the 1D intensity profile along the y_R-axis at each x_R follows:

$$\frac{\langle\psi_{R,H}(x_R)|y_R|\psi_{R,H}(x_R)\rangle}{\langle\psi_{R,H}(x_R)|\psi_{R,H}(x_R)\rangle} = \mp\frac{\cot\theta_I}{2\pi}\mathrm{Re}\left(\frac{\cos\theta_R(x)}{\cos\theta_I(x)}+\frac{r_s^0}{r_p^0}\right), \tag{11a}$$

$$\frac{\langle\psi_{R,V}(x_R)|y_R|\psi_{R,V}(x_R)\rangle}{\langle\psi_{R,H}(x_R)|\psi_{R,H}(x_R)\rangle} = \mp\frac{\cot\theta_I}{2\pi}\mathrm{Re}\left(\frac{\cos\theta_R(x)}{\cos\theta_I(x)}+\frac{r_p^0}{r_s^0}\right), \tag{11b}$$

where the braket integrates the inner expression along the y_R-axis for a fixed x_R, instead of the entire x_R-y_R plane, as in conventional cases. In short, at a curved cloaked surface with a 1D nonlinear phase gradient, the linearly polarized incidence that is split into two opposite circularly polarized components exhibits x_R-dependent displacement along the y_R-axis (Fig. 2(d)). The amount of splitting is related to the local incident and reflected angles ($\theta_I(x)$ and $\theta_R(x)$), and consequently, to the height profile $h(x)$ and phase $\Phi(x)$ (Fig. 2(c)).

As explained earlier, the discordance between the spin Hall shift at the cloaked surface and that at its uncloaked counterpart originates from $\theta_I \neq \theta_R$. This conforms to the fact that Eqs. (10) and (11) differ from Eq. (8) only by the first expression inside the parenthesis that contains only θ_I and θ_R. Therefore, by measuring the SHEL at the two surfaces, we can quantify θ_I, θ_R, ϕ, and h and consequently detect whether the surface is cloaked. Our approach, however, is devised exclusively for the 1D skin cloak and is not applicable to other optical cloaking techniques such as transformation optics because the detection principle relies on a single reflection process and the inequality of the incident and reflected angles.

2.4. Numerical demonstration at the cloaked surface with the linear phase gradient

To numerically demonstrate the SHEL at a cloaked surface, the angular spectrum method

$$\tilde{\boldsymbol{\psi}}(\vec{r}\,') = \mathcal{F}^{-1}\left[\mathcal{F}[\tilde{\boldsymbol{\psi}}(\vec{r})]e^{ik_z z'}\right], \tag{12}$$

is used, where $\mathcal{F}$ is the Fourier transform and $k_z = \sqrt{k_0^2 - k_x^2 - k_y^2}$. At the interface $\vec{r} = (x,\ y,\ z)$, the Jones matrix is multiplied in real space as

$$\tilde{\boldsymbol{\psi}}_R(\vec{r}) = \mathcal{J}(\vec{r})\tilde{\boldsymbol{\psi}}_I(\vec{r}), \tag{13}$$

to address spatially nonuniform reflection coefficients at the interface. Note that the $\vec{k}$ dependence of $\mathcal{J}$ is neglected as $k_0^2 w_0^2 \gg \cot^2\theta_I$ (which enforces $k_x/k_0 \ll 1$). First, we examine a planar surface with a linear phase gradient. For numerical confirmation, the complex reflection coefficients, r_p^0 and r_s^0, are randomly assigned as $r_p^0 = 0.314\exp(-i0.456\pi)$ and $r_s^0 = 0.466\exp(-i0.054\pi)$ (Fig. 3(a)) and then multiplied by a linear phase factor as $r_{p,s}(x) = r_{p,s}^0 e^{i\phi x}$ (Fig. 3(b)). The parameters are given as $\lambda = 633$ nm, $w_0 = 50\lambda$, $\tilde{\theta}_I = 25^\circ$, and $h = x\tan 10^\circ$. To make this surface be perceived as flat, we use $\phi = 0.31k_0$ according to [8] $\triangle\phi = -2k_0 h\cos\tilde{\theta}_I + \pi$, which gives $\theta_I = 15^\circ$ and $\theta_R = 35^\circ$ (Eq. (9)). A spatial area of 0.15 µm × 0.15 µm (approximately $4.74\ w_0 \times 4.74\ w_0$) is considered, and the propagation distance is 5λ for both incident and reflected beams. The intensity profile of the reflected beam proves that the incidence is split into two circularly polarized components along the y_R-axis oppositely (Fig. 3(c)). The splitting is indistinguishable by the human eye because of its subwavelength scale but can be detected experimentally with high precision by adopting weak amplification [19]. The spin Hall shifts obtained by taking y position average of the reflected beam agree perfectly with the analytical value obtained by Eq. (10) under both horizontal and vertical polarizations (Figs. 3(d) and (e)). The spin Hall shifts at the cloaked and uncloaked surfaces are different, proving that the SHEL is a viable candidate for detecting optical cloaking in a nondestructive manner. The numerical estimation can deviate from the analytical value due to the discretization by up to $\pm dx/2$ where dx is the spatial grid size in the simulation (indicated by the error bars in Figs. 3(d) and (e)) and the deviation can be reduced by decreasing dx (Fig. 3(f)).

2.5. Revealing the cloaked surface with a linear phase gradient

This section presents two individual scenarios for revealing an unknown cloaked surface by measuring its SHEL (Table 1). First, we consider a cloaked surface with $r_{p,s}(\vec{k}_I, \vec{r}) = r^0_{p,s}(\vec{k}_I)e^{i\phi x}$ where $r^0_{p,s}$ and ϕ are unknown (Fig. 1(d)). This surface cannot be distinguished from its uncloaked counterpart with $r^0_{p,s}$ and a different slope angle via simple observation (Fig. 1(e)). However, analyzing the SHEL of the beam reflected at the two surfaces under a given polarization (either horizontal or vertical) provides a route to distinguish them (Method 1 in Table 1). Without loss of generosity, we set the incident polarization as horizontal. Subsequently, because δ_H/λ at the cloaked and uncloaked surfaces are distinct (Eqs. (8a) and (10a)), the two surfaces can be discriminated by comparing their SHEL. Indeed, this is a solvable problem because the number of known equations (Eqs. (8a) and (10a)) and unknown variables (θ_I and $\mathrm{Re}(r^0_s/r^0_p)$) are the same. One can find straightforwardly from Eqs. (8a) and (10a) that the local incident angle can be obtained explicitly as

$$\theta_I = \cot^{-1}\left[\frac{2\pi\delta^+_H/\lambda + \sin 2\tilde{\theta}_I}{2\pi\tilde{\delta}^+_H/\lambda \cot\tilde{\theta}_I - \cos 2\tilde{\theta}_I + 1}\right], \tag{14}$$

where $\tilde{\delta}^+_H$ is the spin Hall shift of the LCP component at the uncloaked counterpart. The local reflected angle and phase gradient can be obtained using $\theta_R = 2\tilde{\theta}_I - \theta_I$ and $\phi = k_0(\sin\theta_R - \sin\theta_I)$, respectively. As a proof-of-concept, we demonstrate that θ_I, θ_R, and ϕ of a planar surface with a linear phase gradient can be identified (Fig. 4). The parameters are the same as in the previous study ($\lambda = 633$ nm, $w_0 = 50\lambda$, $\tilde{\theta}_I = 25°$, $h = x\tan 10°$, and $\phi = 0.31k_0$). First, for a given surface, δ is computed numerically using the angular spectrum method (Section 2.4). Then, we assume that only λ and $\tilde{\theta}_I$ are known, whereas the other parameters are unknown. θ_I is deduced using Eq. (14), from which θ_R can be directly obtained (Fig. 4(a)). These results prove that θ_I and θ_R can be estimated successfully. The incident and reflected angles differ from each other due to the nonzero phase gradient along the x-axis (Fig. 4(b)). The estimation of θ_I and θ_R also allows us to evaluate ϕ (Fig. 4(c)).

Table 1. Two techniques to reveal the cloaked surface.

	Method 1 (Uncloaked counterpart exists)		Method 2 (Only the cloaked surface exists)
Incident polarization	Horizontal	Vertical	Both
Measurement target	δ_H at the cloaked/uncloaked surfaces	δ_V at the cloaked/uncloaked surfaces	δ_H and δ_V at the cloaked surface
Corresponding equations	Eqs. (8a) and (10a) for a planar cloaked surface; Eqs. (8a) and (11a) for a curved cloaked surface	Eqs. (8b) and (10b) for a planar cloaked surface; Eqs. (8b) and (11b) for a curved cloaked surface	Eqs. (10a) and (10b) for a planar cloaked surface; Eqs. (11a) and (11b) for a curved cloaked surface
Known variables	$\tilde{\theta}_I$	$\tilde{\theta}_I$	$\tilde{\theta}_I$, $\lvert r_p\rvert$ and $\lvert r_s\rvert$
Unknown variables	θ_I and $\mathrm{Re}(r^0_s/r^0_p)$	θ_I and $\mathrm{Re}(r^0_p/r^0_s)$	θ_I and $\arg(r^0_s/r^0_p)$

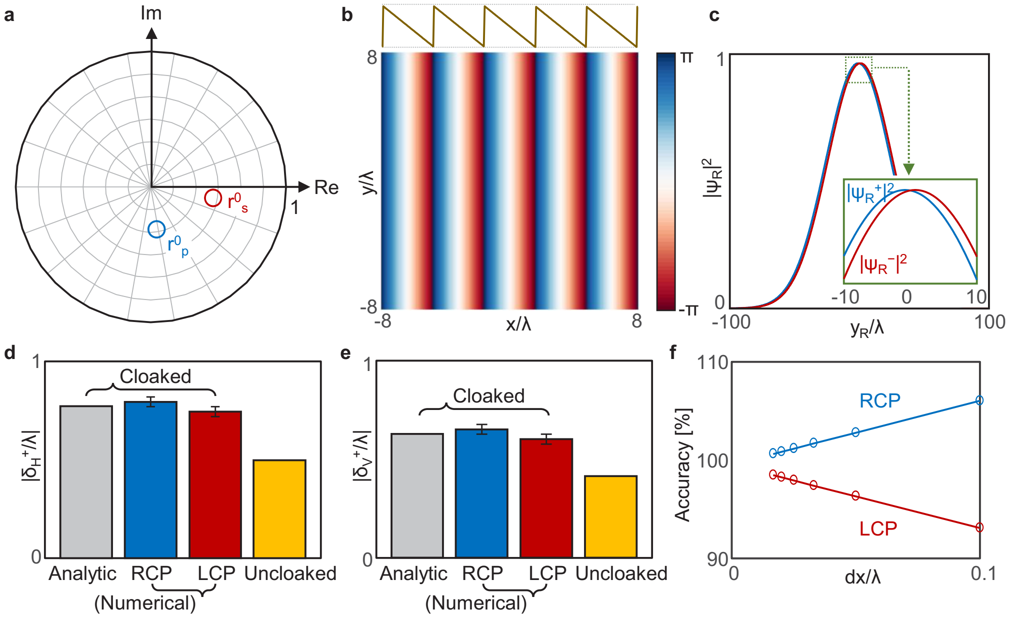

Fig. 3. Numerical simulation of the SHEL at the cloaked surface with linear phase gradient. (a) Randomly assigned reflection coefficients r_p^0 (blue) and r_s^0 (red) represented in the complex plane. (b) Polarization-independent phase ϕx, where $\phi = 0.31k_0$, at the interface. (c) Intensity profile of the reflected beam along the y_R-axis under horizontally polarized incidence. (d, e) Magnitude of the spin Hall shift normalized by wavelength ($|\delta/\lambda|$) under (d) horizontally and (e) vertically polarized incidence calculated analytically (Eq. (10), gray) and by taking y position average of LCP (blue) and RCP (red) at the cloaked surface. Yellow shows the analytic spin Hall shift of the uncloaked counterpart ($\phi = 0$, Eq. (8)). Error bars denote the spatial grid size. (f) Accuracy of the numerical simulation evaluated by the numerical $|\delta_H/\lambda|$ divided by the analytic one.

A limitation of this technique is that there should be an uncloaked surface with the same $r^0_{p,s}$ for comparison. Cloaking can still be unveiled without the uncloaked counterpart by measuring the SHEL under two linear polarizations, horizontal and vertical (Method 2 in Table 1), and their efficiencies. Given that the amplitudes of the reflection coefficients, $|r_p|$ and $|r_s|$, can be deduced from the efficiency of the SHEL [31] ($\epsilon_H = |r_p|^2$ and $\epsilon_V = |r_s|^2$), two unknown variables (θ_I and $\arg(r_s^0/r_p^0)$) can be identified from the SHEL under two linear polarizations at the cloaked surface. The local incident angle can be calculated as follows:

$$\theta_I = \cot^{-1}\left[\frac{2\pi\delta_H^+/\lambda + \sin 2\tilde{\theta}_I}{\cos 2\tilde{\theta}_I}\,\frac{\alpha - \eta^2}{\alpha(\eta^2 - 1)}\right], \tag{15}$$

where $\eta = |r_s/r_p|$ and

$$\alpha = \frac{2\pi\delta_H^+/\lambda + \sin 2\tilde{\theta}_I}{2\pi\delta_V^+/\lambda + \sin 2\tilde{\theta}_I}. \tag{16}$$

Other parameters, such as θ_R and ϕ, can be obtained similarly to Method 1. The results of Method 2 for the same given parameters agree perfectly with those of Method 1 but are not shown here because they are the same as in Fig. 4. The detection of the 1D cloaked surface is also possible by examining the change in the beam waist (see Fig. 2(a)). However, our SHEL-based method provides a precise and quantitative investigation by combining it with a weak measurement.

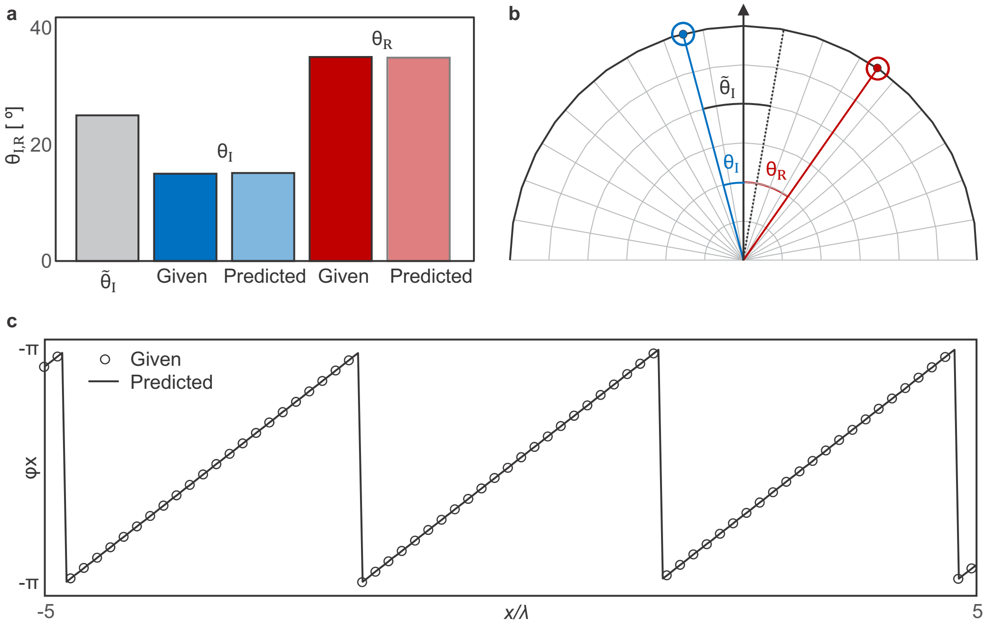

Fig. 4. Revealing the cloaked surface with linear phase gradient using the SHEL. (a) $\tilde{\theta}_I$ (gray), given (dark) and predicted (light) θ_I and θ_R and (b) their graphical illustration. (c) Given (solid) and predicted (markers) phase ϕx of the interface.

These two methods can be generalized to identify cloaked surfaces with a 1D nonlinear phase gradient by conducting the same process for each x_R point. In this a case, $d\Phi/dx = k_0(\sin\theta_R - \sin\theta_I)$, from which full information on the height profile can be deduced. Detailed results are presented in the following section.

2.6. Revealing a cloaked surface with a nonlinear phase gradient

This section demonstrates that the height profile of a curved surface with a nonlinear phase gradient can be identified by investigating SHEL. The angular spectrum method presented in Section 2.4 is used to calculate the spin Hall shift at the curved surface. Because the transformation between the local and central frames can be applied purely in neither $\vec{r}$- nor $\vec{k}$-space and the Fourier transform between x and k_x and that between y and k_y are mutually independent, the beam is expressed as $\tilde{\psi}(x,z)\psi(k_y)$ during the coordinate transformations. The computation area is 1.24 mm × 1.24 mm (approximately 40 $w_0 \times 40\ w_0$), and the height profile of the cloaked surface is assigned as $h(x) = 10\lambda\sin(2\pi x/p + \pi/4)$ where $p = 400\lambda$. The other parameters are given the same.

The numerically obtained spin Hall shifts perfectly match the theoretical values (Eq. (11)) under both horizontal and vertical polarizations (Figs. 5(a) and (b), black curves and markers). The cloaked surface can be detected by comparing the SHEL at the cloaked surface with that at the uncloaked planar counterpart (blue). In addition, the local incident and reflected angles (θ_I and θ_R) and, importantly, the height profile ($h(x)$) can be obtained by analyzing the SHEL of the reflected beam along the x_R-axis (Figs. 5(c) and (d)). For the numerical demonstration, Method 2, shown in Table 1, is applied at each x point. The predicted values of θ_I and θ_R (Fig. 5(c)) and h (Fig. 5(d)) show excellent agreement with the given. The crossing points of the black and blue curves do not indicate the failure of this detection method but imply that the local phase gradient at these points is zero, as confirmed by the zero slope of $h(x)$ (Fig. 5(d)). Note that h can be obtained only as a relative value instead of an absolute one; the numerical result of h shown in Fig. 5(d) is translated to have a center at zero. In real measurements, the reflected beam signal at $|x_R|>2w_0$ (equivalent to $|x_R|>100\lambda$) is extremely low and the results in this regime may not be accurate. The detection area can be widened using incidence with a larger beam waist.

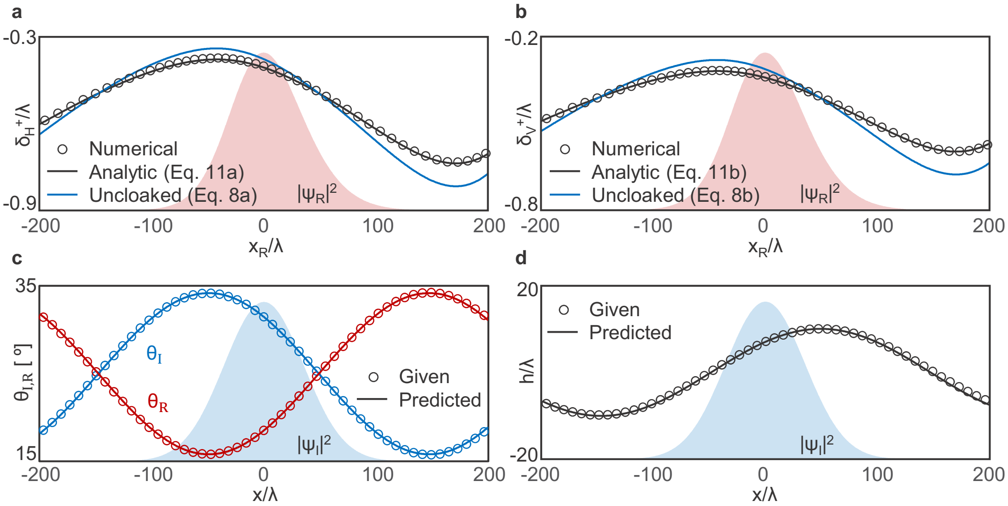

Fig. 5. Revealing the cloaked surface with nonlinear phase gradient using the SHEL. (a, b) Spin Hall shift under (a) horizontal and (b) vertical polarizations at each x_R. Black curves and markers represent analytic and numerically obtained spin Hall shifts. Blue curves show that at uncloaked surface with the same reflection coefficients (Eq. (8)) as a reference. Background profiles are the intensity profile of the reflected beam. (c, d) Given (solid) and predicted (markers) (c) θ_I and θ_R and (d) height. Background profiles are the intensity profile of the incident beam.

3. Conclusion

In conclusion, we have demonstrated that the SHEL can reveal an optical interface with a 1D phase gradient from its illusion with a different geometric shape. The inequality of the incident and reflected angles in this 1D cloaked surface differentiates the SHEL at the cloaked surface from that at its uncloaked counterpart. The SHEL at the optical interface with either a linear or nonlinear 1D phase gradient is theoretically studied, followed by numerical confirmation. Two methods to reveal the incident angle and phase gradient of an unknown cloaked interface are presented. This detection based on SHEL will be a powerful technique to confront optical camouflage or illusion.

Funding. National Research Foundation of Korea (NRF-2022R1C1C2004662, NRF-2022R1F1A1065453).

Disclosures. The authors declare no conflicts of interest.

Data availability. No data were generated or analyzed in the presented research.

References

1. J. B. Pendry, D. Schurig, and D. R. Smith, "Controlling electromagnetic fields," Science **312**(5781), 1780–1782 (2006).
2. U. Leonhardt, "Optical conformal mapping," Science **312**(5781), 1777–1780 (2006).
3. A. Alù and N. Engheta, "Achieving transparency with plasmonic and metamaterial coatings," Phys. Rev. E **72**(1), 016623 (2005).
4. A. Alù and N. Engheta, "Multifrequency optical invisibility cloak with layered plasmonic shells," Phys. Rev. Lett. **100**(11), 113901 (2008).

5. B. Edwards, A. Alù, M. G. Silveirinha, and N. Engheta, "Experimental verification of plasmonic cloaking at microwave frequencies with metamaterials," Phys. Rev. Lett. **103**(15), 153901 (2009).
6. J. Zhang, Z. Lei Mei, W. Ru Zhang, F. Yang, and T. Jun Cui, "An ultrathin directional carpet cloak based on generalized snell's law," Appl. Phys. Lett. **103**(15), 151115 (2013).
7. H. Chu, Q. Li, B. Liu, J. Luo, S. Sun, Z. H. Hang, L. Zhou, and Y. Lai, "A hybrid invisibility cloak based on integration of transparent metasurfaces and zero-index materials," Light: Sci. Appl. **7**(1), 50 (2018).
8. X. Ni, Z. J. Wong, M. Mrejen, Y. Wang, and X. Zhang, "An ultrathin invisibility skin cloak for visible light," Science **349**(6254), 1310–1314 (2015).
9. N. Yu, P. Genevet, M. A. Kats, F. Aieta, J.-P. Tetienne, F. Capasso, and Z. Gaburro, "Light propagation with phase discontinuities: Generalized laws of reflection and refraction," Science **334**(6054), 333–337 (2011).
10. Y. Yang, L. Jing, B. Zheng, R. Hao, W. Yin, E. Li, C. M. Soukoulis, and H. Chen, "Full-polarization 3d metasurface cloak with preserved amplitude and phase," Adv. Mater. **28**(32), 6866–6871 (2016).
11. H.-X. Xu, G. Hu, Y. Wang, C. Wang, M. Wang, S. Wang, Y. Huang, P. Genevet, W. Huang, and C.-W. Qiu, "Polarization-insensitive 3d conformal-skin metasurface cloak," Light: Sci. Appl. **10**(1), 75 (2021).
12. D. Shin, Y. Urzhumov, Y. Jung, G. Kang, S. Baek, M. Choi, H. Park, K. Kim, and D. R. Smith, "Broadband electromagnetic cloaking with smart metamaterials," Nat. Commun. **3**(1), 1213 (2012).
13. K. Tsakmakidis, O. Reshef, E. Almpanis, G. Zouros, E. Mohammadi, D. Saadat, F. Sohrabi, N. Fahimi-Kashani, D. Etezadi, R. Boyd, and H. Altug, "Ultrabroadband 3d invisibility with fast-light cloaks," Nat. Commun. **10**(1), 4859 (2019).
14. X. Tian, J. Xu, T.-H. Xiao, P. Ding, K. Xu, Y. Du, and Z.-Y. Li, "Broadband generation of polarization-immune cloaking via a hybrid phase-change metasurface," Photonics **9**(3), 156 (2022).
15. C. Huang, J. Yang, X. Wu, J. Song, M. Pu, C. Wang, and X. Luo, "Reconfigurable metasurface cloak for dynamical electromagnetic illusions," ACS Photonics **5**(5), 1718–1725 (2017).
16. X. G. Zhang, W. X. Jiang, H. L. Jiang, Q. Wang, H. W. Tian, L. Bai, Z. J. Luo, S. Sun, Y. Luo, C.-W. Qiu, and T. J. Cui, "An optically driven digital metasurface for programming electromagnetic functions," Nat. Electron. **3**(3), 165–171 (2020).
17. C. Qian, B. Zheng, Y. Shen, L. Jing, E. Li, L. Shen, and H. Chen, "Deep-learning-enabled self-adaptive microwave cloak without human intervention," Nat. Photonics **14**(6), 383–390 (2020).
18. M. Onoda, S. Murakami, and N. Nagaosa, "Hall effect of light," Phys. Rev. Lett. **93**(8), 083901 (2004).
19. O. Hosten and P. Kwiat, "Observation of the spin Hall effect of light via weak measurements," Science **319**(5864), 787–790 (2008).
20. X. Ling, X. Zhou, K. Huang, Y. Liu, C.-W. Qiu, H. Luo, and S. Wen, "Recent advances in the spin Hall effect of light," Rep. Prog. Phys. **80**(6), 066401 (2017).
21. X. Yu, X. Wang, Z. Li, L. Zhao, F. Zhou, J. Qu, and J. Song, "Spin Hall effect of light based on a surface plasmonic platform," Nanophotonics **10**(12), 3031–3048 (2021).
22. M. Kim, Y. Yang, D. Lee, Y. Kim, H. Kim, and J. Rho, "Spin Hall effect of light: From fundamentals to recent advancements," Laser Photonics Rev. **17**, 2200046 (2023).
23. S. Liu, S. Chen, S. Wen, and H. Luo, "Photonic spin Hall effect: fundamentals and emergent applications," Opto-Electronic Sci. **1**(7), 220007 (2022).
24. K. Y. Bliokh, C. T. Samlan, C. Prajapati, G. Puentes, N. K. Viswanathan, and F. Nori, "Spin-Hall effect and circular birefringence of a uniaxial crystal plate," Optica **3**(10), 1039–1047 (2016).
25. X. Zhou, X. Ling, Z. Zhang, H. Luo, and S. Wen, "Observation of spin Hall effect in photon tunneling via weak measurements," Sci. Rep. **4**(1), 7388 (2014).
26. T. Tang, C. Li, and L. Luo, "Enhanced spin Hall effect of tunneling light in hyperbolic metamaterial waveguide," Sci. Rep. **6**(1), 30762 (2016).
27. O. Takayama, J. Sukham, R. Malureanu, A. V. Lavrinenko, and G. Puentes, "Photonic spin Hall effect in hyperbolic metamaterials at visible wavelengths," Opt. Lett. **43**(19), 4602–4605 (2018).
28. M. Kim, D. Lee, T. H. Kim, Y. Yang, H. J. Park, and J. Rho, "Observation of enhanced optical spin Hall effect in a vertical hyperbolic metamaterial," ACS Photonics **6**(10), 2530–2536 (2019).
29. M. Kim, D. Lee, B. Ko, and J. Rho, "Diffraction-induced enhancement of optical spin Hall effect in a dielectric grating," APL Photonics **5**(6), 066106 (2020).
30. Y. Yang, T. Lee, M. Kim, C. Jung, T. Badloe, D. Lee, S. Lee, H.-J. Lee, and J. Rho, "Dynamic optical spin Hall effect in chitosan-coated all-dielectric metamaterials for a biosensing platform," IEEE J. Sel. Top. Quantum Electron. **27**(5), 1–8 (2021).
31. M. Kim, D. Lee, H. Cho, B. Min, and J. Rho, "Spin Hall effect of light with near-unity efficiency in the microwave," Laser Photonics Rev. **15**(2), 2000393 (2021).
32. M. Kim, D. Lee, T. H.-Y. Nguyen, H.-J. Lee, G. Byun, and J. Rho, "Total reflection-induced efficiency enhancement of the spin Hall effect of light," ACS Photonics **8**(9), 2705–2712 (2021).
33. M. Kim, D. Lee, and J. Rho, "Spin Hall effect under arbitrarily polarized or unpolarized light," Laser Photonics Rev. **15**(7), 2100138 (2021).
34. M. Kim, D. Lee, Y. Yang, Y. Kim, and J. Rho, "Reaching the highest efficiency of spin Hall effect of light in the near-infrared using all-dielectric metasurfaces," Nat. Commun. **13**(1), 2036 (2022).

35. M. Kim, D. Lee, and J. Rho, "Incident-polarization-independent spin Hall effect of light reaching half beam waist," Laser Photonics Rev. **16**(6), 2100510 (2022).
36. M. Kim, D. Lee, Y. Kim, and J. Rho, "Generalized analytic formula for spin Hall effect of shift enhancement and interface independence," Nanophotonics **11**(11), 2803–2809 (2022).
37. M. Kim, D. Lee, Y. Kim, and J. Rho, "Nanophotonic-assisted precision enhancement of weak measurement using spin Hall effect of light," Nanophotonics **11**(20), 4591–4600 (2022).
38. X. Zhou, X. Ling, H. Luo, and S. Wen, "Identifying graphene layers via spin Hall effect of light," Appl. Phys. Lett. **101**(25), 251602 (2012).
39. J. Liu, K. Zeng, W. Xu, S. Chen, H. Luo, and S. Wen, "Ultrasensitive detection of ion concentration based on photonic spin Hall effect," Appl. Phys. Lett. **115**(25), 251102 (2019).
40. S. Chen, X. Ling, W. Shu, H. Luo, and S. Wen, "Precision measurement of the optical conductivity of atomically thin crystals via the photonic spin Hall effect," Phys. Rev. Appl. **13**(1), 014057 (2020).
41. X. Zhou, L. Sheng, and X. Ling, "Photonic spin Hall effect enabled refractive index sensor using weak measurements," Sci. Rep. **8**(1), 1221 (2018).
42. J. Cheng, G. Wang, P. Dong, D. Liu, F. Chi, and S. Liu, "Photonic spin Hall effect and terahertz gas sensor via insb-supported long-range surface plasmon resonance," Chin. Phys. B **31**(1), 014205 (2022).
43. B. Wang, K. Rong, E. Maguid, V. Kleiner, and E. Hasman, "Probing nanoscale fluctuation of ferromagnetic meta-atoms with a stochastic photonic spin Hall effect," Nat. Nanotechnol. **15**(6), 450–456 (2020).
44. R. Wang, J. Zhou, K. Zeng, S. Chen, X. Ling, W. Shu, H. Luo, and S. Wen, "Ultrasensitive and real-time detection of chemical reaction rate based on the photonic spin Hall effect," APL Photonics **5**(1), 016105 (2020).
45. J. Cheng, Y. Xiang, J. Xu, S. Liu, and P. Dong, "Highly sensitive refractive index sensing based on photonic spin Hall effect and its application on cancer detection," IEEE Sens. J. **22**(13), 12754–12760 (2022).
46. N. Li, T. Tang, J. Li, L. Luo, C. Li, J. Shen, and J. Yao, "Highly sensitive biosensor with graphene-mos2 heterostructure based on photonic spin Hall effect," J. Magn. Magn. Mater. **484**, 445–450 (2019).
47. H. Luo, X. Ling, X. Zhou, W. Shu, S. Wen, and D. Fan, "Enhancing or suppressing the spin Hall effect of light in layered nanostructures," Phys. Rev. A **84**(3), 033801 (2011).
48. H. Luo, X. Zhou, W. Shu, S. Wen, and D. Fan, "Enhanced and switchable spin Hall effect of light near the brewster angle on reflection," Phys. Rev. A **84**(4), 043806 (2011).
49. K. Y. Bliokh and A. Aiello, "Goos–hänchen and imbert–fedorov beam shifts: an overview," J. Opt. **15**(1), 014001 (2013).